University of Groningen

Bachelor Research Project 23/24

Study of $\Lambda_b^0 \to \Lambda^0\ \mu^+\mu^-$ at low q^2

Author:
Tim van der Meer
Student Number:
S4907906

Supervisor:
dr. A. (Ann-Kathrin) Perrevoort
Second Examiner:
prof. dr. S. (Steven) Hoekstra

July 21, 2024

The rare $\Lambda_b^0 \to \Lambda^0\ \mu^+\mu^-$ decay is studied and the possibility of measuring a non-zero branching fraction is discussed. The study introduces a normalisation mode $\Lambda_b^0 \to \Lambda^0 J/\psi\ (\to \mu^+\mu^-)$ used to find the branching fraction of the dimuon mode. An efficiency representing the mismatch between the number of total and observed events is calculated. A hyper Gaussian function fit is used to model expected detector data signal with Monte Carlo simulated events. The signal model shows a disparity between the fitted function and the reconstructed mass spectrum as the number of events predicted by the integral under the fit do not match the actual number of simulated events. Real detector data fitting is unsuccessful. Improvements could include more consistent analysis methods, machine learning algorithms, researching and modelling backgrounds as well as utilising a truth matching method.

Contents

1 Introduction

Over the course of history, scientists sought out to comprehend everything there is to understand about the universe, taking steps in the realms of both the tangible and the intangible. Nowadays, physicists often deal with theories and experiments involving the smallest scales and the highest energies, here the *Standard Model of particle physics (SM)* is regarded as the pinnacle of our understanding of elementary particles. Although it works well enough in the subatomic domain, the model fails to incorporate gravity as well as leaving major questions about the early universe unanswered [1]. Additionally, numerous decay measurements of the bottom quark, which together with other quarks and leptons make up the smallest known building blocks of matter, have hinted at coherent deviations from Standard Model predictions [2]. Examples are the $b \to s\,\ell\,\ell$ and the $b \to c\,\ell\,v_\ell$ modes, where a bottom quark decay into strange quark and a dilepton pair, or into a charm quark, a lepton and its neutrino [3]. These decays are mediated by the *weak force*, one of the four fundamental forces of nature. This will be discussed in more detail in the next section.

This incomplete theory and the possible anomalies sparked the notion of physics *Beyond the Standard Model (BSM)*. Getting closer to BSM requires extensive testing of the SM, where predicted numbers and properties are compared with data obtained from the detectors such as those at the *Large Hadron Collider (LHC)* [4]. A detector that specifically aims to record the decay of particles containing this bottom quark is the LHCb detector [5]. One of the fundamental SM properties which is being studied thoroughly at LHCb is *Lepton Flavour Universality (LFU)*. LFU states that the weak force carriers couple equally to the different lepton generations [6]. Furthermore, LFU is accidentally conserved by the SM, but nothing prevents BSM from violating it. It is however not possible to conclusively state that BSM at play at the SM "deviations".

A specific decay used by the LHCb collaboration to test the SM, which is also the topic of interest for this thesis, is the $\Lambda_b^0 \to \Lambda^0\mu^+\mu^-$ mode. This decay mode of the bottom quark containing baryon is rare and displays the aforementioned SM deviation of the $b \to s\,\ell\,\ell$ mode. A differential branching fraction measurement for different q^2 of this mode has been performed by the LHCb collaboration. Here, q^2 refers to the momentum transfer to the dilepton pair. Measurements from an earlier data set was observed to be consistent with the predictions in the high-q^2 region. In the low-q^2 region however, below the J/ψ meson for $0.1 < q^2 < 8$ GeV^2/c^4, the same cannot be said [7]. Current measured differential branching fractions in the low q^2 region are stated in table 1.

q^2 interval (GeV^2/c^4)	Diffential branching fraction (GeV^2/c^4)$^{-1}$
$1.0 < q^2 < 6.0$	$(4.7^{+3.1}_{-2.7}) \cdot 10^{-8}$
$6.0 < q^2 < 8.0$	$(5.0 \pm 2.5) \cdot 10^{-8}$

Table 1: Current measured differential branching fractions of $(\Lambda_b^0 \to \Lambda^0\ \mu^+\mu^-)$ [8].

The aim of this thesis is to study the $\Lambda_b^0 \to \Lambda^0\mu^+\mu^-$ decay at low-q^2, investigating the possibility of measuring a branching fraction larger than zero with additional data from Run-2. This study will provide a more in-depth discussion of the Standard Model, Lepton Flavour Universality, branching fractions and dilepton invariant mass spectra. The LHCb detector at the LHC will be addressed. Finally, the approach to analyse, and results obtained from both simulation and real data will be presented and discussed.

2 Theory

2.1 The Standard Model of Particle Physics

The *Standard Model of Particle Physics (SM)* is regarded as one of the greatest achievements of modern physics. With increasing investments in time and resources on the high-energy frontier during the 20th century, scientists were able to construct a coherent model of the known elementary particles. The SM describes, excluding gravity, the fundamental particles and interactions that constitute visible matter of the universe.

The first fundamental building blocks are the *quarks.* The six different flavoured quarks always come in pairs, or *generations.* The up, charm and top quarks, collectively referred to as *up-type*, possess a charge of $+\frac{2}{3}e$ whereas the three *down-type* quarks have a $-\frac{1}{3}e$ charge. Here, e is the elementary charge. With these constituents the *hadrons* may come into existence. Hadrons are bound states of quarks that possess a charge that is a multiple of e. The most common hadrons are the baryons consisting of three quarks, anti-baryons consisting of three anti-quarks and the mesons consisting of a quark and an anti-quark. An antiparticle has the opposite quantum numbers as the normal particle, but its mass is exactly the same.
The other group of particles that make up the SM are the *leptons*, these come like the quarks in generations. In every generation, there exists a negatively charged lepton (electron (e^-), muon (μ^-) or the tau particle(τ^-)) that is accompanied by the respective neutral lepton neutrino (v_e, v_μ or v_τ). All leptons have an anti-particle as well.

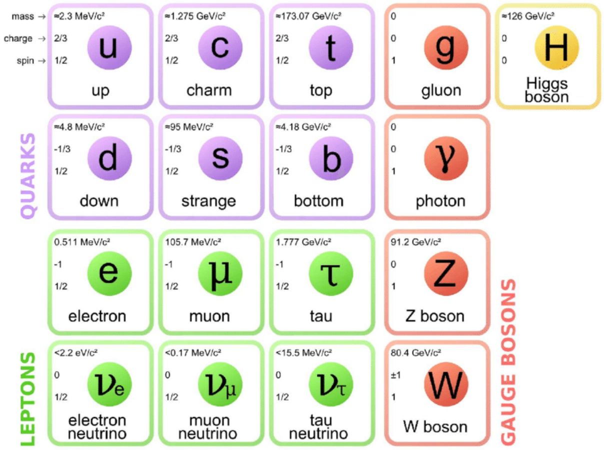

Figure 1: The standard Model of particle physics [9].

All aforementioned fundamental particles form the spin $\frac{1}{2}$ *elementary fermions.* In addition to those there are the spin 1 *elementary bosons*, the four gauge bosons incorporated in the SM are force carriers, or mediators of the fundamental interactions. The electromagnetic interaction is mediated by the photon (γ), the electroweak interaction is mediated by the charged $W^\pm$ and the neutral Z gauge bosons, lastly the strong interactions are governed by gluons. The strong force only interacts with (anti)quarks and the electromagnetic force can also interact with charged leptons. The electroweak force can interact with quarks and all leptons, this will be discussed in more detail in the following subsection. A new scalar boson, which was coined the Higgs boson, was predicted in 1964 [10] and its measurement has been verified in 2013. The Higgs boson, which is a mediator of the Higgs field, is responsible for giving mass to some of the elementary particles [11]. The whole Standard Model is often summarized in the form of figure 1.

2.2 Electroweak interactions

Unlike the electromagnetic and strong force, all fermions can interact with the weak force. These interaction involve *Charged Currents (CC)* and *Neutral Currents (NC)* through the exchange of $W^{\pm}$ and Z bosons respectively. The weak decay that will be of interest in this study is the $b \to s\,\ell\,\ell$ mode. This is an example of a *Flavour Changing Current*, where the initial quark decays to a different flavour quark and a charged lepton, anti-lepton pair.
This flavour changing can occur via *Flavour Changing Charged Currents (FCCC)*. A $W^{\pm}$ boson couples to the initial quark resulting in another quark that is possibly from another generation. This process can either go from an up- to a down-type quark, or the other way around. The coupling strength and specifics of the quarks interacting with these charged bosons are governed by the *Cabibbo-Kobayashi-Maskawa (CKM) matrix* [12]. The CKM matrix suggests that the coupling strength is larger within the generations.
A property that occurs for $W^{\pm}$ bosons is *helicity suppression*. This is a consequence of the boson only being able to interact with left-handed particles and right-handed anti-particles [12].
Another type of quark flavour change occurs through *flavor-changing neutral currents (FCNC)*. The initial and final quark are now of the same 'type', possessing the same charge. The neutral Z boson can not change the flavour of a quark, hence the SM forbids a FCNC. Instead, a process like this would occur via a loop diagram (figure 2a), with many coupling constants entering in the full transition making it a highly suppressed mode [13].

(a) A $b \to s\mu\mu$ FCNC decay via a loop Feynman-Diagram (allowed by the SM)

(b) A $b \to s\mu\mu$ FCNC decay via a BSM Z' (not allowed in the SM)

Figure 2: Standard Model contribution to the $b \to s\mu\mu$ transition (a) and a hypothetical BSM Z' contribution (b) [14].

2.3 Lepton Flavour Universality and BSM physics

The SM of particle physics demands that the electroweak force mediators couple equally strong to the three different lepton families. This phenomenon is known as *Lepton Flavour Universality (LFU)*. The only contributions that would then affect the branching fraction ratios are the available *phase space* and helicity suppression [15].
A clearly measured violation of this phenomenon could suggest the possibility of beyond standard model contributions to the transition. Hints of SM deviations have been found which led to the postulation of different models that could justify them. The prime model that can adress most, if not all, anomalies contains the so-called *leptoquarks*, which are hypothetical particles that have shared interactions with both quarks and leptons [16]. An other model, which can be seen in figure 2b, offers a Z' gauge boson as a mediator of the weak force [17]. Unlike its unprimed SM counterpart, this boson is allowed to directly couple to the different quarks in a flavour changing event. Both of these models open up a new understanding of reality, although conclusively stating that the bottom quark transition is affected by BSM theories is not yet possible. Current experiments have not definitively observed a LFU violation, the general expectation of is that this could be within experimental reach. The promising modes for LFU testing at the LHC include the following modes [18]: $b \to s\ \ell\ell$, $b \to c\ \ell\nu$ and $b \to s\ \bar{\nu}\nu$.

2.4 Dilepton invariant mass

A concept that is often encountered is the *dilepton invariant mass*, denoted by $m_{\ell\ell}$. It is given by:

$$m_{\ell^+\ell^-} = \frac{1}{c}\sqrt{\frac{(E_{\ell^+} + E_{\ell^-})^2}{c^2} - \|\mathbf{p}_{\ell^+} + \mathbf{p}_{\ell^-}\|^2} \tag{1}$$

Where $E_{\ell^{+/-}}$ and $\mathbf{p}_{\ell^{+/-}}$ are respectively the energy and momentum of the lepton, c is the speed of light. Rewriting equation 1 yields the following invariant mass squared, often refereed to as q^2:

$$q^2 = m^2_{\ell^+\ell^-} = \frac{1}{c^2}\left(\left(\frac{E_{\ell^+} + E_{\ell^-}}{c}\right)^2 - \|\mathbf{p}_{\ell^+} + \mathbf{p}_{\ell^-}\|^2\right) \tag{2}$$

When defining the *four momentum* of a lepton as $p^{\mu}_{\ell^{+/-}} = (E_{\ell^{+/-}}/c,\ \mathbf{p}_{\ell^{+/-}})$, it can be seen that equation 2 might be written as $q^2 = 1/c^2\ (p_{\ell^+} + p_{\ell^-})^{\mu}(p_{\ell^+} + p_{\ell^-})_{\mu}$. In other words, the q^2 value is the square magnitude of the four momentum vector with a $1/c^2$ factor that accounts for the units, it is often associated with the momentum transfer to the lepton pair.

2.5 The Λ_b^0 baryon and branching fractions

The Λ_b^0 (udb) baryon and its $\Lambda_b^0 \to \Lambda^0\ \ell^+\ell^-$ decay mode make up one of the LFU testing grounds. It nicely complements other $b \to s\ \ell\ \ell$ LFU tests that currently look SM-like

[19]. The specific transition and the possibility of measuring the *branching fraction* that will be of interest in this thesis is the dimuon decay:

$$\Lambda_b^0 \to \Lambda^0\ \mu^+\mu^-$$

The branching fraction is the fraction of decays via a certain mode compared to all possible decay modes:

$$\mathcal{B}_i = \frac{N_i}{\sum_j N_j}$$

In this case, it would be the number (N) of dimuon decays compared to the total number of other decays ($N(H_i)$), i.e.:

$$\mathcal{B}\left(\Lambda_b^0 \to \Lambda^0\ \mu^+\mu^-\right) = \frac{N(\Lambda_b^0 \to \Lambda^0\ \mu^+\mu^-)}{\sum_i N(\Lambda_b^0 \to H_i)} \tag{3}$$

An arising problem is that the denominator of equation 3 requires the the measurement of all possible Λ_b^0 decays simultaneously. The short decay time of Λ_b^0 leads to the fact that this particle can only be identified by backtracking decay products to a possible mother. Backgrounds and other errors would make this process a very inconsistent one if all mothers were to be found.
As a solution, an extra Λ_b^0 decay mode with a known branching fraction that acts as a normalisation mode will be introduced:

$$\Lambda_b^0 \to \Lambda^0\ J/\psi(\to \mu^+\mu^-)$$

With:

$$\mathcal{B}\left(\Lambda_b^0 \to \Lambda^0\ J/\psi(\to \mu^+\mu^-)\right) = \frac{N\left(\Lambda_b^0 \to \Lambda^0\ J/\psi(\to \mu^+\mu^-)\right)}{\sum_i N(\Lambda_b^0 \to H_i)} \tag{4}$$

In this new mode the J/ψ is a $c\bar{c}$ resonance with an extremely short lifetime. To avoid future confusion, this will henceforth be called normalisation mode and $\Lambda_b^0 \to \Lambda^0\ \mu^+\mu^-$ the dimuon mode. Equation 3 and 4 share the unknown denominator, which means that the following can be obtained after rearranging:

$$\mathcal{B}\left(\Lambda_b^0 \to \Lambda^0\ \mu^+\mu^-\right) = \frac{N(\Lambda_b^0 \to \Lambda^0\ \mu^+\mu^-)}{N\left(\Lambda_b^0 \to \Lambda^0\ J/\psi(\to \mu^+\mu^-)\right)} \mathcal{B}\left(\Lambda_b^0 \to \Lambda^0\ J/\psi(\to \mu^+\mu^-)\right) \tag{5}$$

In figure 3 a schematic of the decay can be seen, the figure provides a zoom in of the first vertex after the primary vertex. In the dimuon mode, the ends of the muon arrows meet at this second vertex. For the normalisation mode, an extra arrow is drawn between the second vertex and the base of the muon arrows.

With this lifetime the detector will work with a dimuon pair regardless of the intermediate J/ψ. this state also sets the upper limit of the low q^2 region. A way to distinguish the dimuon decay from the normalisation mode is by considering the dimuon invariant mass. Ensuring that the decay products of the dimuon mode give a total invariant mass equal

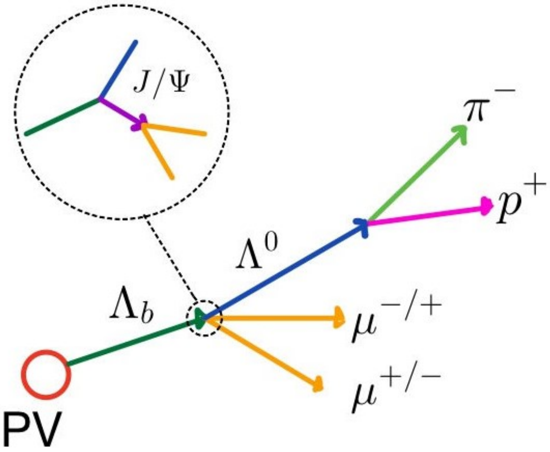

Figure 3: Topology of the Λ_b^0 decay including the normalisation mode.

to the Λ_b^0 mass, the lower and upper q^2 limit are given by: $4m_\mu^2 < q^2 < (m_{\Lambda_b^0} - m_{\Lambda^0})^2$, or $0.045 < q^2 < 20.280$ GeV^2/c^4. This corresponds to a relatively broad $m_{\mu\mu}$ spectrum. On the other hand, the invariant mass of the muons in the normalisation mode must be equal to the mass of their mother, which is the J/ψ state. Therefore, this $m_{\mu\mu}$ distribution shows a narrow peak centered at the J/ψ mass. Both distributions are displayed in figures 4a and 4b.

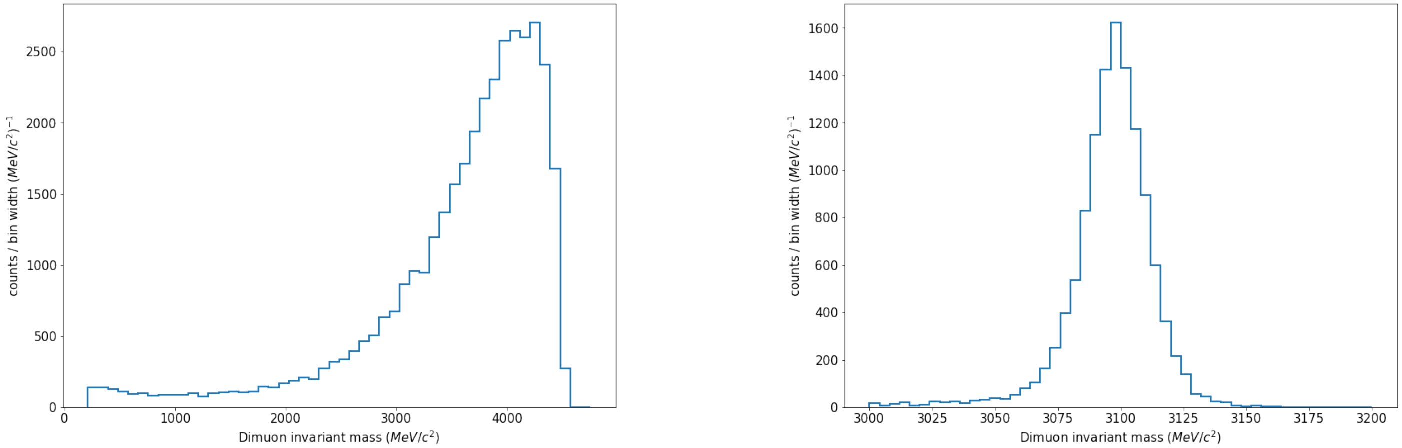

(a) Dimuon invariant mass spectrum of the dimuon mode according to simulation data

(b) Dimuon invariant mass spectrum of the normalisation mode according to simulation data

Figure 4: Simulation data displaying the expected distribution for both the dimuon and normalisation mode.

3 The LHCb detector at LHC

3.1 The Large Hadron Collider

The *Large Hadron Collider (LHC)* is the largest particle accelerator in the world. Two tubes kept at an ultrahigh vacuum use strong magnetic fields to guide protons close to lightspeed in antiparallel directions before they are made to collide. These collisions happen at four different positions around the accelerator ring, corresponding to the four particle detectors: ATLAS [20], CMS [21], ALICE [22], and LHCb.

CERN started the LHC experiment in 2008 and it has received different upgrades along the way. At the LHC, there are different data taking periods, called runs. This study will focus on data from Run 2, which was from 2015 to 2018. This run started a few years after Run 1, which ran from 2011 to 2013. The goal of the second run is to increase the data quality compared to the first run, possibly gaining more insight in certain uncharted physical phenomena.
During Run 1 the beam energy was around 3.5 TeV yielding a center of mass energy ($\sqrt{s}$) of 7 TeV. This center of mass energy was nearly doubled for Run 2. To increase the chance of particle collision, a proton beam consists of orderly spaced proton packets, also referred to as *bunches*. The bunch separation determines the LHCb detector input rate. A 50 ns separation during Run 1 gave a 20 MHz input rate, this input rate was doubled for Run 2. The luminosity of a particle accelerator is a quantity that measures the ability to produce the required number of interactions. This makes it the proportionality factor between the number of events per unit time and the proton-proton reaction cross section σ_{pp}. It has the unit $\mathrm{cm}^{-2}\,\mathrm{s}^{-1}$ [23]. The peak luminosity during Run 1 was $7 \cdot 10^{33}\ \mathrm{cm}^{-2}\,\mathrm{s}^{-1}$. During Run 2 this quantity was nearly tripled, which means that the number of interactions per crossing also saw an increase.
The LHC parameter values during both runs are stated in the table below [24].

LHC parameter	Unit	Run 1	Run 2
E_{cm} ($\sqrt{s}$)	[TeV]	7	13
Bunch separation	[ns]	50	25
Peak $\mathcal{L}$	[$\mathrm{cm}^{-2}\mathrm{s}^{-1}$]	$7 \cdot 10^{33}$	$2 \cdot 10^{34}$
Interactions[1]	-	≈ 21	≈ 55

[1] Interactions refer to interactions per crossing at peak Luminosity

3.2 The LHCb detector

The $b \to s\ \mu^+\mu^-$ transition is being researched at the LHCb detector. Compared to the other three detectors at LHC, which surround the entire collision point with layers of sub detectors, the LHCb experiment has a different geometry. This unique shape is called a single forward-arm detector, one that is built like a cone instead of layered sphere. The shape of the detector is justified by the fact that the hadrons formed by the *pp collisions*

stay close to the line of the beam pipe.
LHCb has several sub-detectors, each specialised in measuring different characteristics of the reaction products. The whole detector can be seen in figure 5. Together, the components can collect data regarding several properties of the produced particles.

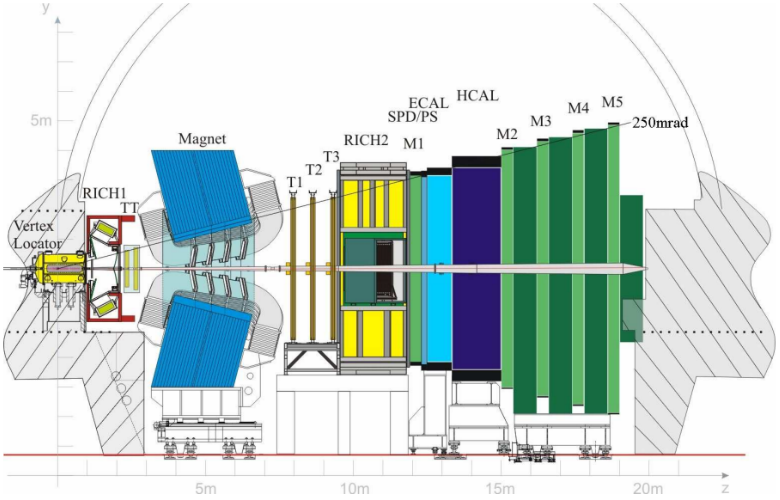

Figure 5: Side view of the LHCb detector [5].

The vertex locator (VELO) is the first instrument in the detector and its purpose is to provide precise measurements of track coordinates close to the interaction region. These are then used to identify displaced secondary vertices ([5], ch 5.1). The VELO consists of two movable detector halves and operates in a vacuum in order to minimize the amount of material between the sensors and the interaction point. Both halves of the VELO are equipped with multiple modules that consist of two micro-strip silicon sensors to measure R and ϕ perpendicular to the beam axis. The required aperture increases during the injection of the proton beam into the LHC , the two halves are retracted [25]. A dipole magnet with an integrated magnetic field of 4 Tm is used to measure the momentum of charged particles.

Between the VELO and the magnet is one of the two Silicon Trackers (ST), this the Tracker Turencis (TT). The main purpose of this component is to improve the momentum resolution for charged particles as well as increasing long-lived neutral particles reconstruction efficiency ([5], ch 5.2), which decay outside of the VELO.

In the LHCb detector are also two Ring Imaging Cherenkov counters (RICH 1-2). Cherenkov radiation occurs when a particle moves faster than the phase velocity of light in a medium. The detectors measure the velocity of the particles. RICH1 is located before the TT and it covers the low momentum charged particle range of 1-60 GeV/c. RICH2 is located after the (T1-T3) tracking stations and covers the high momentum rang from 15 GeV/c up to and beyond 100 GeV/c ([5], ch 6.1). Together with the momentum measurements of charged particles and the mass, a *particle identification (PID)* is obtained.

Further downstream are the electronic and hadronic calorimeters: ECAL and HCAL. They select transverse energy hadron, electron and photon candidates for the first trigger level (L0) of the detector and provide information about the identity, position and energies of particles that will be analysed. In front of the calorimeters are scintillation pads, SPD and PS. These components help with distinguishing properties of particles. Doing so decreases the background in the muon detectors.

The muon system consists of 5 stations (M1-M5). Station 1 is placed in front of the calorimeters and is used to improve the transverse momentum measurement. The other four stations are placed downstream of the calorimeters and have 80 cm thick iron absorbers placed in between, these stop hadrons that reached this part of the detector. Together, the detectors provide space point measurements of the tracks ([5], ch 6.3).

LHCb is able to reconstruct several track categories, the most relevant are the *long tracks (LL)* and the *downstream tracks (DD)*. The first uses hits from all tracking systems and the latter combines hits from the TT and and the three tracking stations [26]. With roughly 1TB of data generated per second, means to store and analyse all LHCb data is not feasible with the current state of technology. Therefore scientists use a *trigger*, which is an event selection procedure, to reach the desired scientific goals. During the second run, this trigger consisted of two parts: the *hardware trigger*, which is a combination of fast electronics, and the *software trigger*, consisting of computer algorithms [27].

3.3 Background effects

The precision of a measurement in particle physics depends very much on the available computing power and algorithms that can accurately reconstruct the decay process or other relevant parameters from the decay products. To obtain results, candidates from the desired transition ought to be singled out from the 'noise'. There are certain possible factors which affect the measurement uncertainty.

High track densities in the detector pose a challenge for track reconstruction, leading to *ghost tracks*. These tracks do not belong to a physical process, they are a consequence of random hit combinations, wrongfully formed during the pattern recognition step [28].

A second error comes from *combinatorial background*. There are many transitions happening but take for example the many $J/\psi \to \mu^+\mu^-$ decays in the detector. The detector reconstructs a muon and anti-muon that have a combined invariant mass closely equal to that of J/ψ to a common vertex. This makes them a dimuon pair. However, it may be possible that these muons did not come from the same mother particle. Given the vast number of decays that happen and reconstructions that occur, a lot of combinatorial background may accumulate in the data.

Another source of background is a particle *mis-identification*. This refers to particles that have been incorrectly identified by the detector systems. Causes for this could be a similarity in the produced signal by different particles or a limitation in the resolution of the detector. Another background source are *partially reconstructed tracks*. These occur when all the required information to fully reconstruct the particle is not available. Lastly, there are other semi-leptonic decays that mimic the signal, during reconstruction a certain part of the distribution will consist of other unwanted modes.

4 Approach and results

Returning to the concluding paragraph of the introduction, this study aims to study the feasibility of measuring the $\Lambda_b^0 \to \Lambda^0\ \mu^+\mu^-$ decay at low q^2. In other words, is it possible to obtain a branching fraction for this transition that is larger than zero. As the branching fraction of the normalisation mode is known, the first consideration is the fraction in equation 5. In this equation, the number of events for both decay modes represents the actual, or total number of decays (N_T). It is only possible to observe a fraction (N_O) of these due to several factors which will be addressed in the following subsection. The two quantities are related by the *efficiency (ϵ)*, where: $N_O = \epsilon\ N_T$, the efficiency is always less than or equal to unity. This turns equation 5 into the following:

$$\frac{\mathcal{B}\,(\Lambda_b^0 \to \Lambda^0\ \mu^+\mu^-)}{\mathcal{B}\,(\Lambda_b^0 \to \Lambda^0\ J/\psi(\to \mu^+\mu^-))} = \frac{N_O(\Lambda_b^0 \to \Lambda^0\ \mu^+\mu^-)}{N_O\,(\Lambda_b^0 \to \Lambda^0\ J/\psi(\to \mu^+\mu^-))} \cdot \frac{\epsilon_{\Lambda_b^0 \to \Lambda^0\ J/\psi(\to\mu^+\mu^-)}}{\epsilon_{\Lambda_b^0 \to \Lambda^0\ \mu^+\mu^-}} \tag{6}$$

The goal is then to obtain the two counts and efficiencies. To gain more insight in these numbers, Monte Carlo (MC) simulations were used, which simulate the pp-collisions. The number of events that can be created in a MC simulation is limited due to the available computer resources. Instead of simulating pp-collisions with all possible interactions, selected modes such as the dimuon, normalisation and other (semi) leptonic modes are simulated. The number of simulated events does not necessarily match the number of events in the recorded data and therefore needs proper scaling. Additionally, it is not possible to perfectly simulate the real experiment. A set of *weights*, explicitly stated in appendic 6, is applied to account for the differences, these weights introduce errors.

4.1 Obtaining efficiencies

The total efficiency (ϵ) means how many real decays can be counted in an analysis after all selections, it is composed of three of efficiencies that can be determined from MC data. The generator level efficiency (ϵ_{gen}) refers to the fraction of potential decay events that are actually simulated during the MC simulation process. Simulating every possible event is computationally expensive and so simulation is restricted to events that are likely to be detected. This efficiency represents the proportion of events that are simulated out of all possible events within the relevant phase space region where they could potentially end up in the detector.

A second efficiency, the reconstruction efficiency (ϵ_{rec}), measures the detector's and algorithms' ability to correctly identify and reconstruct the particle tracks from the decay events. Not every particle produced in a decay will create detectable signals in the detector. Lastly, there is the selection efficiency (ϵ_{sel}). In order to increase signal purity, different selections are imposed on the the simulated decay modes. These selections are meant to increase the relative occurrence of desired simulated decay modes.

The latter two effiencies can be written as:

$$\epsilon_{rec} = \frac{\text{Number of reconstructed events}}{\text{Number of requested events}} \tag{7}$$

$$\epsilon_{sel} = \frac{\text{Number of events passing all selections}}{\text{Number of reconstructed events}} \tag{8}$$

Hence, a new combined efficiency (ϵ_{com}) can be defined, it is equal to the product of these two:

$$\epsilon_{com} = \frac{\text{Number of events passing all cuts}}{\text{Number of requested events}} \tag{9}$$

For every year (2016-2018) and for both the dimuon and normalisation mode, the number of events after cutting and weights, the number of requested events and the generator level efficiency can be found. With those a new efficiency can be defined, this is the product of the generator level efficiency and the combined efficiency and shall be denoted as $\epsilon_{\text{mode}}^{\text{year}}$. From here the final efficiency that is unknown in equation 6 can be found with the following formula:

$$\epsilon_{\text{mode}} = \sum_{year} \epsilon_{\text{mode}}^{\text{year}} \mathrm{w}_{\mathcal{L}}(\text{year}) \tag{10}$$

Here, $\mathrm{w}_{\mathcal{L}}$ is the luminosity weight. That is a factor assigned to each MC sample to reflect the relative portion of the total integrated luminosity that the experiment operated in different configurations such as different years or magnet polarities. It makes sure that the simulation accurately represents the conditions during the actual data-taking period. The mode is either the dimuon mode ($\Lambda_b^0 \to \Lambda^0\ \mu^+\mu^-$) or the normalisation mode ($\Lambda_b^0 \to \Lambda^0\ J/\psi(\to \mu^+\mu^-)$).

Now the goal is to obtain suitable selections, the number of requested events, the generator level efficiencies and yearly luminosity's.

A simulation containing both modes of interest, as well as several dimuon background processes is put together. In order to obtain the efficiencies it must be known what part, or fraction of the desired decay is present compared to all other modes. The first goal is to map all the events in the regions of interest. These will be the low q^2 region with $4m_\mu^2 < q^2 < 8$ GeV^2/c^4 and the J/ψ region with 8 GeV^2/c$^4 < q^2 < 11$ GeV^2/c^4, in this report also referred to as the high q^2 region.

A total of eight different samples, all LL tracks with a MU magnet polarisation from 2018 were simulated and weighted. The luminosity is not considered for this part of the analysis as all MC samples are from the same year and posses the same magnet polarisation, they therefore have the same luminosity.

The goal now is to find suitable selections that suppress the amount of background modes more than the desired mode in a region. These selections are tested by imposing them on the same number of events for all modes.

After applying weights, all number of events before any selections were measured for all the modes. After this a total number of events, equal for all modes in the region was chosen. For low q^2 this was 5000 and for high q^2 it is 15000. With this number a scaling can be obtained, this scaling factor can give every mode that many events. This puts the number of counts prior to imposing selections for different events on equal footing. After that, selections can be applied in the different regions. After selections, the number of events passing all selection can be observed. Due to the scaling factor, every sample had selections applied to the same number of initial counts. Then, for every sample, the number of remaining counts can be observed. With this, the effect of the imposed selections can be used to observe the suppression on the desired modes compared to the background modes. The re scaled data without any applied selections is shown in figures 6a and 6b. Without errors, all samples have an equal number of counts.

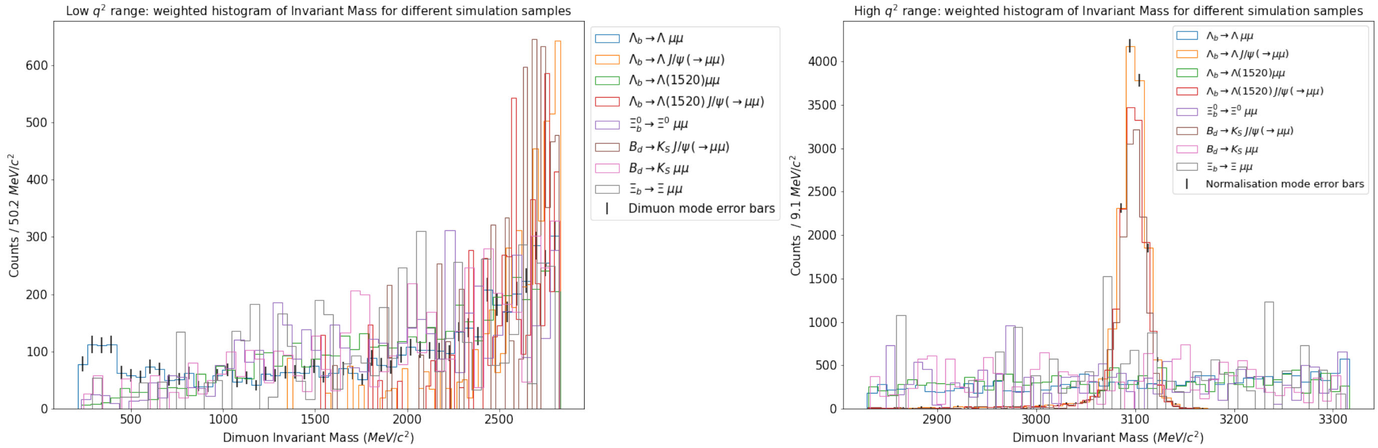

(a) Dimuon invariant mass spectrum in the low q^2 region for simulated samples. Each sample has 5000 events in this range

(b) Dimuon invariant mass spectrum in the high q^2 region for simulated samples. Each sample has 15000 events in this range

Figure 6: Before selections imposed dimuon invariant mass spectra for weighted samples in low and high q^2 regions. For the sake of visibility, only the error bars of the dimuon and normalisation mode are shown.

In order to minimise the the effects of other modes that mimic the signal, certain selections must be imposed on the data that will increase the relative occurrences of the desired modes. The first selection is a transverse momentum cut on the long tracks: all charged hadrons from an LL track must have a transverse momentum greater than $0.5\ GeV/c$. This includes the pion and proton that originate from the Λ_0 as well as both muons from the muon pair. The long tracks (LL) include information from the VELO and therefore offer a better precision in determining the particle's trajectory and momentum. The VELO is located close the primary vertex, meaning that this region has a high track density. Among these tracks are many lower-energy particles. By imposing a momentum selection on the LL-tracks, low momentum tracks more likely to be noise are excluded which increases the purity.
Next, the Λ_0 mass of a reconstructed Λ_0 candidate must be within 20 MeV/c^2 of the world average Λ_0 mass which is roughly 1115 $\mathrm{MeV/c^2}$.
For the next part of the analysis the reconstruction of the Λ_b^0 mass will play a role. The world average Λ_b^0 mass sits roughly at 5619 $\mathrm{MeV/c^2}$, a loose selection is set at $5500\ \mathrm{MeV/c^2} < m_{\Lambda_b^0} < 5740\ \mathrm{MeV/c^2}$. Additional selections that have shown to increase the data yield are particle identification selections on the proton and the pion. Other selections put on the Λ_b^0 are an upper limit to the baryons travel distance before decaying,

and the condition that the Λ_b^0 reconstruction must have a good χ^2 value. A full overview of the selection ntuples used in the code can be found in appendix 6.
With the selections imposed on data, a new figure constructed. From the 5000 events in the low q^2 and 15000 events in the high q^2 region, the events passing all selections are plotted in figures figures 7a and 7b.

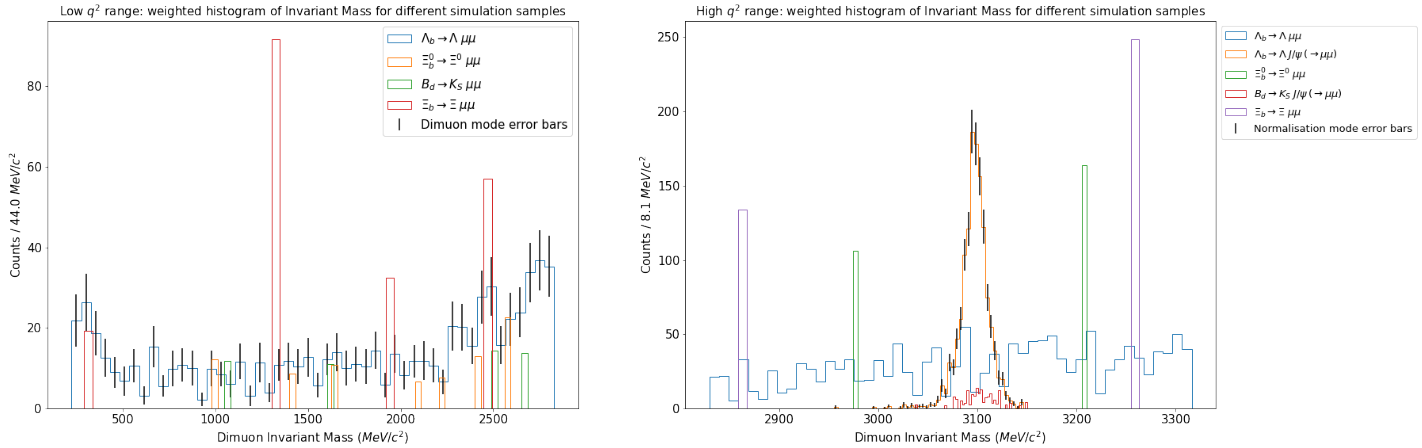

(a) Dimuon invariant mass spectrum in the low q^2 region for simulated samples

(b) Dimuon invariant mass spectrum in the high q^2 region for simulated samples

Figure 7: Selection imposed dimuon invariant mass spectra for weighted samples in low and high q^2 regions. For the sake of visibility, only the error bars of the dimuon and normalisation mode are shown. Some samples had no events passing all selections, hence they are not present in the plots.

With these figures, a table 2 can be constructed:

	Low q2		High q2	
Sample	Events before	Events after	Events before	Events after
$\Lambda_b \to \Lambda\ \mu\mu$	5000 ± 100	692±34	15000 ± 332	1434±91
$\Lambda_b \to \Lambda\ J/\psi\,(\to \mu\mu)$	5000 ± 383	-	15000 ±144	1320 ± 38
$\Lambda_b \to \Lambda(1520)\mu\mu$	5000 ± 126	-	15000 ± 552	-
$\Lambda_b \to \Lambda(1520)\ J/\psi\,(\to \mu\mu)$	5000 ± 619	-	15000 ± 234	-
$\Xi_b^0 \to \Xi^0\ \mu\mu$	5000 ± 303	82±34	15000 ±1532	271 ±195
$B_d \to K_S\ J/\psi\,(\to \mu\mu)$	5000 ± 974	-	15000 ± 326	171 ±27
$B_d \to K_S\ \mu\mu$	5000 ± 330	51±26	15000 ± 1460	-
$\Xi_b \to \Xi\ \mu\mu$	5000 ± 503	200±25	15000 ± 2407	383 ± 283

Table 2: Number of events before and after applying selections. The '-' indicates that there are no events that passed the selections

With these suitable selections, the next steps of finding the efficiency can be taken. For both the analysis of the simulation data as well as real data used to obtain a result in the end, all data types will be used. What this means is that every combination (year, track,

magnet polarity) for 2016, 2017 or 2018 data will be considered.
Starting off with the simulation data. The efficiency for both modes of interest can be found by finding the number of events passing the selections, the number of requested events, the generator level efficiency and the luminosity for each year and each mode. After that, equation 10 is used to find the final efficiency for both modes.
For both modes, a total of twelve different samples are analysed and $\epsilon_{\text{mode}}^{\text{year}}$ is computed by finding the product of the combined efficiency with the generator level efficiency. The number of requested events for each year is $3 \cdot 10^6$. The total efficiency $\epsilon_{\text{mode}}^{\text{year}}$ as well as the luminosity weight from each year are stated in table 3, generator level efficiencies are roughly 20 % [29]. The luminosity weight from the three years follow $\sum_{year} \text{w}_{\mathcal{L}} = 1$. Combining $\epsilon_{\text{mode}}^{\text{year}}$) and the luminosity's from the table and utilising equation 10, the final efficiency for the dimuon and normalisation mode can be obtained:

	$\epsilon^{\text{year}}_{\Lambda_b^0 \to \Lambda^0\ \mu^+\mu^-}$ (10^{-5})	$\epsilon^{\text{year}}_{\Lambda_b^0 \to \Lambda^0\ J/\psi(\to \mu^+\mu^-)}$ (10^{-5})	$\text{w}_{\mathcal{L}}$
2016	64 ± 4	134 ± 4	0.298
2017	63 ± 4	136 ± 4	0.309
2018	69 ± 4	130 ± 4	0.393

Table 3: Efficiency and luminosity weight of the dimuon and normalisation modes for different years.

$$\epsilon_{\Lambda_b^0 \to \Lambda^0\ \mu^+\mu^-} = (66 \pm 2) \cdot 10^{-5}$$
$$\epsilon_{\Lambda_b^0 \to \Lambda^0\ J/\psi(\to \mu^+\mu^-)} = (133 \pm 2) \cdot 10^{-5}$$

4.2 Signal Modelling

The next part of the analysis will focus on finding the observed number of decays for both transitions, this is done by optimizing a function through the reconstructed Λ_b^0 mass diagram of MC samples. In the simulation, the number of reconstructed Λ_b^0 baryons is known. When plotting the reconstructed Λ_b^0 mass, a peak around the 'true' mass will form. As there is no combinatorial background present in the simulations, an expected signal shape distribution can be obtained. A best fit through this histogram of expected data can be made, after which this shape can be applied to an actual data set.
The area below the curve of the best fit is related to and the number of bin heights and bin widths. The Riemann sum tells that the sum of the products between the height and width of all bins approximates the integral under a curve, given that there are enough bins. Both of these quantities can be optimized with simulation data, given that both the height and width can be adjusted in the simulation.
After that the purity of the fit is considered. In the simulation, the exact number of events that pass all cuts is known, and therefore the number of events predicted by fit can be compared to it.

A multitude of functions, including a Gaussian, Lorentzian and Breit-Wigner distribution were applied to the MC data. Here it is important to note that different simulation samples are used. The signal modeling was performed with LL tracks from combined 2016, 2017 and 2018 data. The function with the best goodness-of-fit χ^2 statistic was the *hyper gaussian*, which is of the following form:

$$f(x) = a \cdot exp\left(-\left(\frac{x-b}{c}\right)^d\right)$$

Using the standard python optimization package `scipy`, different fits were made to the data. One is optimized to go through the top of the bins in the histogram, the other two will make a fit through the maximum and minimum bin heights respectively. Like with obtaining efficiencies, the MC data contains errors due to the weights. Based on these uncertainties three fits through MC data are calculated. The resulting fits are shown in figure 8a and 8b.

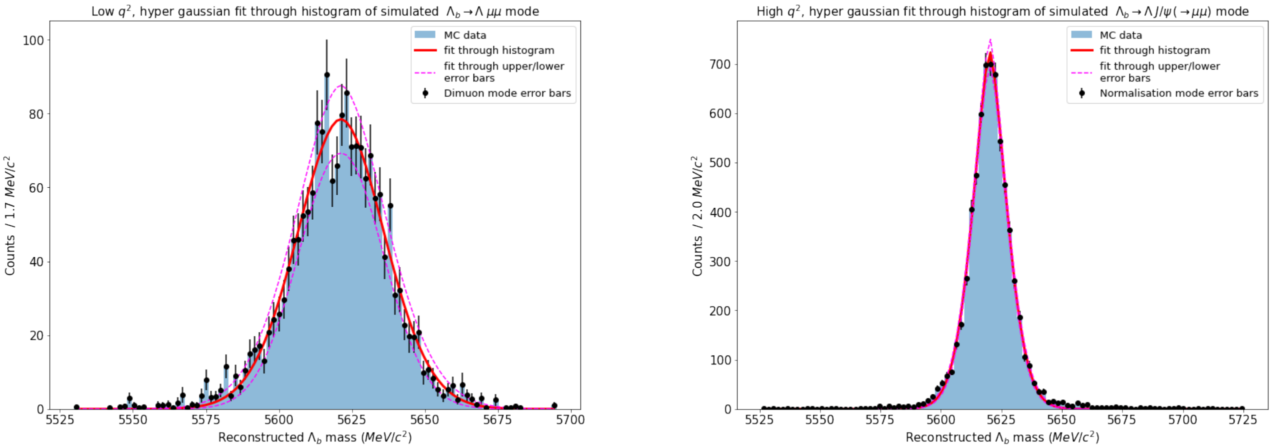

(a) Λ_b^0 reconstructed mass fit in the low q^2 region

(b) Λ_b^0 reconstructed mass fit in the high q^2 region

Figure 8: Hyper Gaussian fit through histogram of simulated dimuon and normalisation modes.

The quantity on the vertical axis displays counts per mass where as the units on the horizontal axis are a mass. The area under the curve fit would be unit less, this is because the product of the integrand and the differential of the variable is unit less too. The integral under the curve can therefore be used to calculate the number of events. The number of events that passed all events can be compared to the number of events predicted by the integral. From this, a correction factor (p) that accounts for the mismatch between the two numbers can be computed. In figure 8 as well as table 4 it can be seen that the integral over estimates the number of events. For this reason an extra correction factor is added to equation 6.

	Low q^2 region	High q^2 region
Events passing selections	2349	8924
Integral	2985 ±468	13010 ± 687

Table 4: Events passing all selections and integral under the curve fit for low and high q^2 region

With results from the table the following correction factors can be computed:

$$1/p_{\Lambda_b^0 \to \Lambda^0\ \mu^+\mu^-} = 1.3 \pm 0.2$$
$$1/p_{\Lambda_b^0 \to \Lambda^0\ J/\psi(\to \mu^+\mu^-)} = 1.5 \pm 0.1$$

4.3 Detector data analysis

With the results from the previous sections, the final detector data results can be studied. In both q^2 regions but especially in the lower, there is a lot of combinatorial background interfering with the desired result. For this reason the distribution is different than the one predicted in the previous subsection. The real data with and without applied selection, as well as the expected distributions are plotted in figures 9a and 9b.

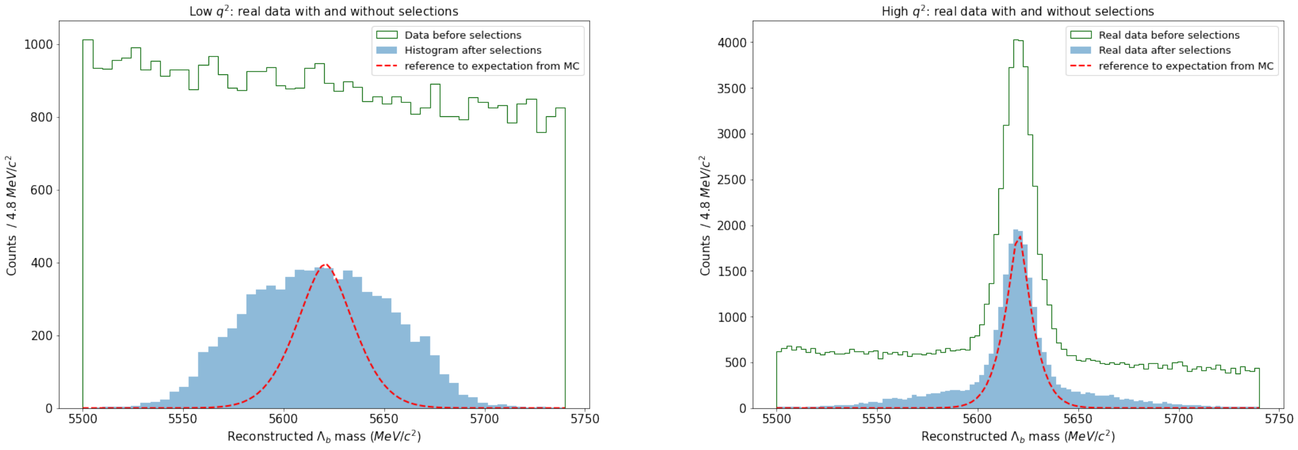

(a) Real data before and after selections for low q^2 region

(b) Real data before and after selections for high q^2 region

Figure 9: Real data, both figures have a plot that shows the MC predicted data distribution for that mode

Proceeding with the data analysis using results from these figures is not scientifically sound as the difference between the predicted and actual data distribution is too large. Although it is more feasible for the high q^2 region to obtain a signal count, it will not be done since a final result cannot be obtained without the result of the low q^2 region. This is to be discussed further in the upcoming section. For now, the final steps that would finish the approach will be addressed.

Suppose the real data, that should have error bars accounting for a statistical uncertainties, can be fitted with the distribution model. Then for both modes a number of observed counts with an error can be obtained. With the additional correction factor, equation 6 is slightly altered:

$$\frac{\mathcal{B}\left(\Lambda_b^0 \to \Lambda^0\ \mu^+\mu^-\right)}{\mathcal{B}\left(\Lambda_b^0 \to \Lambda^0\ J/\psi(\to \mu^+\mu^-)\right)} = \frac{N_O(\Lambda_b^0 \to \Lambda^0\ \mu^+\mu^-)}{N_O\left(\Lambda_b^0 \to \Lambda^0\ J/\psi(\to \mu^+\mu^-)\right)} \cdot \frac{p_{\Lambda_b^0 \to \Lambda^0\ \mu^+\mu^-}}{p_{\Lambda_b^0 \to \Lambda^0\ J/\psi(\to \mu^+\mu^-)}} \cdot \frac{\epsilon_{\Lambda_b^0 \to \Lambda^0\ J/\psi(\to \mu^+\mu^-)}}{\epsilon_{\Lambda_b^0 \to \Lambda^0\ \mu^+\mu^-}}$$

Four of the five variables, besides the unknown number of observed events, have been obtained in the data analysis. The fifth variable is the 'known' branching fraction of the normalisation mode. This value is given by $\mathcal{B}\left(\Lambda_b^0 \to \Lambda^0\ J/\psi(\to \mu^+\mu^-)\right) = (2.67 \pm 0.03 \pm 0.20) \cdot 10^{-4}$ [30], where the first error is statistical and the second systematic.

If N_O of the dimuon and normalisation mode could have been obtained from the abovementioned fit, the branching fraction of the dimuon mode, $\mathcal{B}\left(\Lambda_b^0 \to \Lambda^0\ \mu^+\mu^-\right)$ could be obtained.

5 Discussion

Based on the combined results of both real and simulation data analysis, it can be stated that it is not possible to measure a branching fraction greater than zero for the dimuon decay at low q^2 with the approach described in this report. There are however a few amends that can be made to the approach which may help increase the quality of the results.

In the presented study, only a subset of the available simulation data was used. Moreover, different sets of simulated events were chosen in different parts of the analysis. All samples that were used to obtain suitable selections were taken from 2018 simulation data, with an LL track type and an up-MU detector dipole magnet polarization. The reason for this is related to code runtime, to gain understanding of the MC data and the effect of possible selections on the data distribution all the ntuples from the simulation data were imported. The detector data analysis considers all track type, dipole magnet polarization combinations from three different years. The whole simulation better resembles the data combinations used for the detector data analysis if more sets of simulated events from 2018 are added to the existing simulated events. This could possibly reveal better selections or cut values. Additionally, data from 2016 and 2017 could be considered to increase chosen set of simulated events. Including downstream (DD) tracks to the simulation could improve the sensitivity a bit. Here it is important to note that simulation data best reflects the running conditions during data taking periods. This would not significantly alter the results as running conditions do not change significantly over different years, this also makes the current approach of only using 2018 simulation data acceptable.

For similar code runtime reasons, not all background modes were taken into the total set of simulated events. Among these backgrounds are $\Lambda_b^0 \to \Lambda^0(1600)\ \mu^+\mu^-$, $\Lambda_b^0 \to \Lambda^0(1405)\ \mu^+\mu^-$ and these modes with an intermediate J/ψ. Other simulated modes that were available but not considered are all modes with an intermediate $\Psi(2S)$ state, which is even heavier than the J/ψ. Adding these to the simulation data should also increases the resemblance to real detector data, they were however left out because they were observed to be insignificant. Another consideration could be the influence of non dimuon backgrounds where one or more particles in the chain are misidentified, as explained in section 3.3. This could be a large contributing factor for the shapes seen in figure 9, but likely beyond the reach of this study.

Besides the set of simulated data, there are also other selections that can be used to increase this relative occurrence of a desired simulated mode with respect to other present simulated modes. Examples of these selections are imposing a minimum lifetime on the Λ_b^0 or Λ^0 baryons, or the displacement of the Λ_b^0 from the primary vertex. Like the Λ_b^0, a condition on the χ^2 value of the Λ^0 particle reconstruction can be imposed as well. A final possible adjustment would be a condition concerning the angular spread of decay products, where the angle between the vectors of a mother and daughter particle is not allowed to exceed a certain value.

During the whole analysis, the dimuon and normalisation modes were almost regarded as the same transition, but in a different q^2 region. This is for the reason that both modes have equal selections. Although the largest issue is likely not the data from the

normalisation mode, different selections or cuts optimizing that decay should have been considered. The selections imposed on the dimuon mode appeared to have suppressed its background modes by a strong amount. Due to an error in the code that was only discovered later it can be observed that this is not the case for the normalisation mode. Here, the dimuon mode counts as a background and it occurs roughly as much as the normalisation mode after selections. Tailoring selections to the normalisation mode could yield a stronger suppression of the dimuon and other background modes.
Lastly, during the research of the selections there were no luminosity's considered. As previously mentioned, this is acceptable since all simulation data are LL, MU, 2018. However, when adding different simulation sets the luminosity weights should be considered.

To avoid confusion, in order to determine the selections, different simulation LL, MU, 2018 samples were analysed. The goal of this was to use these to find the number of events that passed all selections. With these selections and some additional data, a total efficiency was computed. The computation of this efficiency was performed with the simulated version of the detector data. Namely, all track and dipole magnet polarization combinations for 2016, 2017 and 2018 simulation data. The data sets used for each part of the data analysis are more clearly stated in appendix 6.

The focus of the second part of the analysis was obtaining a fit that could have been used to obtain results from the actual data set. For both the dimuon and normalisation mode, all LL, MU and LL, MD samples from 2016, 2017 and 2018 simulation files were analysed. Again, no DD samples were used. On top of that, the simulated data for the fit is not equal to the simulated version of the files used for the data used in detector data analysis. For this reason the simulation displays the same distribution, but not quite the same scale.
A second point regarding the fits has to do with the range, the Λ_b^0 mass was required to be within a certain interval, which is also the interval of the plots. As a result, many data points are farther than 3σ from the resonance mass. Especially in the high q^2 plot it can be seen that a lot of data points are in the tail and not in the peak. A smaller range for the data fit could be considered to have a better fit of the peak. Additionally, it is possible that the hyper Gaussian is not the best possible fit for the function and a different fit would yield better results.
Another big improvement concerning the fits is the considering fitting functions of background processes (background modelling) as well as fitting a signal-plus-background-fit.

A key aspect of connecting simulations with actual data is the truth matching method. Truth matching involves using a 'truth' value for a particular particle property to identify all corresponding reconstructed particles. It refers to the process of linking a detector signal to the specific particle being studied. When a reconstructed candidate is truth matched, it means the signals used in the reconstruction originated from the simulated particle, rather than from other particles. To more accurately predict the data in the experiment, correctly weighting and applying the truth matching would be beneficial.

The detector data is is not suitable to be fitted with the signal model. It can be observed that the data after selections distribution in figure 9a is very similar to the base of the selection imposed real data of the normalisation mode in figure 9b. The reason for this is likely presence of combinatorial background, misidentified backgrounds and partially reconstructed decays. More reasonable results can be obtained if these factors are reduced. In order to reject some of the combinatorial backgrounds a small extra analysis was performed. A comparison of a variable distribution was made of the data signal above the Λ_b^0 mass, where the only contribution are backgrounds, to the theoretical distribution of the variable. This way, some variables were found to significantly decrease the backgrounds. A few were found but the most dominant was the `Lb_DTF_Lb_PV_chi2_0` variable, which is the χ^2 of the full Λ_b^0 decay chain. The rest of the figures showing different distributions can be found in appendix 6. Improvements to the Λ_b^0 reconstructed mass spectrum can be made if more of these variables are considered in an analysis. The effects of combinatorial background could also be minimised by implementing a machine learning algorithm that can help reject this data.
Furthermore, researching systematic errors besides the statistical errors could help improve quality of results. Examples of these systematic errors are detector calibration and tracking efficiency.

6 Conclusion

The study analyzed the rare $\Lambda_b^0 \to \Lambda^0\ \mu^+\mu^-$ decay and explored the feasibility of measuring a branching fraction larger than zero. The approach included introducing a normalisation mode ($\Lambda_b^0 \to \Lambda^0 J/\psi\ (\to\ \mu^+\mu^-)$) and obtaining efficiencies as a proportionality factor between the total and observed number of events. Signal modeling with simulation data was used to fit the Λ_b reconstructed mass diagram. This fit, derived from Monte Carlo (MC) data, could be applied to real detector data to obtain the necessary information for calculating the branching fraction.

Efficiencies consist of a generator level efficiency, reconstruction efficiency, and selection efficiency. These, combined with the luminosity weight, provided a final efficiency. For the selection efficiency, various selections were imposed on the MC data to ensure that the desired modes were less suppressed than the background modes. The analysis showed that the backgrounds were more suppressed for the dimuon mode. The dimuon mode was the largest background for the normalisation mode and it is not suppressed enough, indicating a need for better-tailored selections.

The fitting function used was a hyper Gaussian, which had the best chi-square statistic. However, there was a mismatch between the number of events in the reconstructed Λ_b mass spectrum and the integral under the fit. This disagreement could be addressed by carefully choosing integration and fitting bounds, or by selecting a different fit function. The final detector data was too complex to fit a function to, this is likely caused by backgrounds. Machine learning algorithms may be necessary for improvement, as simple selections were insufficient.

The low q^2 region data likely consisted only of backgrounds, misidentified tracks, and partially reconstructed tracks. Improvements could come from introducing background or signal-plus-background fitting to achieve a better signal model for real data. The current approach did not allow for the measurement of the branching fraction, but more consistent methods across different parts of the analysis, including machine learning algorithms and possibly a truth-matching method, could improve the overall results.

References

[1] CERN, *The Standard Model*, last accessed on 14 may 2024, n.d. [Online]. Available: `https://home.cern/science/physics/standard-model`.

[2] LHCb collaboration, “Test of lepton universality in $b \to s l l$ decays,” *Physical Review Letters*, vol. 131, no. 5, Aug. 2023, last accessed on 14 may 2024, ISSN: 1079-7114. DOI: `10.1103/physrevlett.131.051803`. [Online]. Available: `http://dx.doi.org/10.1103/PhysRevLett.131.051803`.

[3] Y. Amhis *et al.*, “Averages of b-hadron, c-hadron, and τ-lepton properties as of 2021,” *Phys. Rev. D*, vol. 107, p. 052 008, 2023. DOI: `10.1103/PhysRevD.107.052008`. arXiv: `2206.07501 [hep-ex]`.

[4] “LHC Machine,” *JINST*, vol. 3, L. Evans and P. Bryant, Eds., S08001, 2008. DOI: `10.1088/1748-0221/3/08/S08001`.

[5] A. A. Alves Jr. *et al.*, “The LHCb Detector at the LHC,” *JINST*, vol. 3, S08005, 2008, last accessed on 10 june 2024. DOI: `10.1088/1748-0221/3/08/S08005`.

[6] S. Celani, *Lepton flavour universality tests and lepton flavour violation searches at lhcb*, last accessed on 18 june 2024, 2021. arXiv: `2111.11105 [hep-ex]`.

[7] L. collaboration, “Differential branching fraction and angular analysis of $\Lambda_b^0 \to \Lambda\mu^+\mu^-$ decays,” *JHEP*, vol. 06, p. 115, 2015, Comments: 27 pages, 10 figures. DOI: `10.1007/JHEP06(2015)115`. arXiv: `1503.07138`. [Online]. Available: `https://cds.cern.ch/record/2003794`.

[8] R. L. Workman *et al.*, “Review of Particle Physics,” *PTEP*, vol. 2022, p. 083C01, 2022, last accessed on 20 july 2024. DOI: `10.1093/ptep/ptac097`.

[9] A. Arbuzov, *Quantum field theory and the electroweak standard model*, last accessed on 14 july 2024, Jan. 2018. [Online]. Available: `https://www.researchgate.net/publication/322568259_Quantum_Field_Theory_and_the_Electroweak_Standard_Model`.

[10] P. W. Higgs, “Broken symmetries and the masses of gauge bosons,” *Phys. Rev. Lett.*, vol. 13, pp. 508–509, 16 Oct. 1964, last accessed on 17 july 2024. DOI: `10.1103/PhysRevLett.13.508`. [Online]. Available: `https://link.aps.org/doi/10.1103/PhysRevLett.13.508`.

[11] CERN, *The Higgs boson*, last accessed on 11 june 2024, n.d. [Online]. Available: `https://home.cern/science/physics/higgs-boson`.

[12] D. Griffiths, *Introduction to Elementary Particles*. New York, USA: John Wiley Sons, 1987, last accessed on 15 july 2024.

[13] S. Playfer and S. Stone, “Rare b Decays,” *International Journal of Modern Physics Letters*, May 1995, last accessed on 11 june 2024. [Online]. Available: `https://arxiv.org/pdf/hep-ph/9505392`.

[14] W. Barter and M. Bradley, *Lhcb experiment looks forward*, Newsletter of the EP Department, CERN, last accessed on 14 june 2024, Mar. 2021. [Online]. Available: https://ep-news.web.cern.ch/content/lhcb-experiment-looks-forward.

[15] Katharina Müller and on behalf of the LHCb Collaboration, "Tests of lepton flavour universality at lhcb," *Journal of Physics: Conference Series*, vol. 1271, no. 1, p. 012 009, Jul. 2019, last accessed on 20 june 2024. DOI: 10.1088/1742-6596/1271/1/012009. [Online]. Available: https://dx.doi.org/10.1088/1742-6596/1271/1/012009.

[16] A. Crivellin, B. Fuks, and L. Schnell, "Explaining the hints for lepton flavour universality violation with three s2 leptoquark generations," *Journal of High Energy Physics*, vol. 2022, no. 6, Jun. 2022, last accessed on 22 june 2024, ISSN: 1029-8479. DOI: 10.1007/jhep06(2022)169. [Online]. Available: http://dx.doi.org/10.1007/JHEP06(2022)169.

[17] A. J. Buras and J. Girrbach, "Left-handed z and z fcnc quark couplings facing new $\mathrm{b} \rightarrow \mathrm{s} +$ data," *Journal of High Energy Physics*, vol. 2013, no. 12, Dec. 2013, last accessed on 14 june 2024, ISSN: 1029-8479. DOI: 10.1007/jhep12(2013)009. [Online]. Available: http://dx.doi.org/10.1007/JHEP12(2013)009.

[18] D. Guadagnoli and P. Koppenburg, "Lepton-flavor violation and lepton-flavor-universality violation in b and c decays," *arXiv preprint arXiv:2207.01851*, 2022, last accessed on 14 june 2024. arXiv: 2207.01851 [hep-ph]. [Online]. Available: https://doi.org/10.48550/arXiv.2207.01851.

[19] T. Gutsche, M. A. Ivanov, J. G. Korner, V. E. Lyubovitskij, and P. Santorelli, "Rare baryon decays $\Lambda_b \to \Lambda l^+ l^- (l = e, \mu, \tau)$ and $\Lambda_b \to \Lambda\gamma$: differential and total rates, lepton- and hadron-side forward-backward asymmetries," *Phys. Rev. D*, vol. 87, p. 074 031, 2013, last accessed on 15 june 2024. DOI: 10.1103/PhysRevD.87.074031. arXiv: 1301.3737 [hep-ph].

[20] G. Aad *et al.*, "The ATLAS Experiment at the CERN Large Hadron Collider," *JINST*, vol. 3, S08003, 2008, last accessed on 20 july 2024. DOI: 10.1088/1748-0221/3/08/S08003.

[21] S. Chatrchyan *et al.*, "The CMS Experiment at the CERN LHC," *JINST*, vol. 3, S08004, 2008, last accessed on 20 july 2024. DOI: 10.1088/1748-0221/3/08/S08004.

[22] K. Aamodt *et al.*, "The ALICE experiment at the CERN LHC," *JINST*, vol. 3, S08002, 2008, last accessed on 20 july 2024. DOI: 10.1088/1748-0221/3/08/S08002.

[23] W. Herr and B. Muratori, "Concept of luminosity," in *CERN Accelerator School: Intermediate Course on Accelerator Physics, Zeuthen, Germany, 15-26 Sep 2003*, D. Brandt, Ed., https://cds.cern.ch/record/941318/files/p361.pdf, CERN, 2006, pp. 361–378, ISBN: 978-92-9083-267-6. DOI: 10.5170/CERN-2006-002.

[24] T. A. Collaboration, "The design and performance of the atlas inner detector trigger for run 2 lhc collisions at s=13 tev," *Journal of Physics: Conference Series*, vol. 762, no. 1, p. 012 029, Oct. 2016. DOI: 10.1088/1742-6596/762/1/012029. [Online]. Available: https://doi.org/10.1088/1742-6596/762/1/012029.

[25] O. Behrendt, "The lhcb vertex locator," *Nuclear Instruments and Methods in Physics Research Section A: Accelerators, Spectrometers, Detectors and Associated Equipment*, vol. 598, no. 1, pp. 61–63, 2009, Instrumentation for Collding Beam Physics, ISSN: 0168-9002. DOI: https://doi.org/10.1016/j.nima.2008.08.111. [Online]. Available: https://www.sciencedirect.com/science/article/pii/S016890020801190X.

[26] A. Perieanu, "Identification of ghost tracks using neural networks," LHCb Note, Tech. Rep. Issue: 1, Dec. 2007, Ref: LHCb 2007-158, last accessed 21 june 2024. [Online]. Available: https://www.physi.uni-heidelberg.de/Forschung/he/LHCb/documents/InternalNotes/IdentGhostNote.pdf.

[27] Large Hadron Collider beauty experiment, *LHCb's unique approach to real-time data processing*, last accessed on 20 june 2024. [Online]. Available: https://lhcb-outreach.web.cern.ch/2023/03/01/lhcbs-unique-approach-to-real-time-data-processing/.

[28] M. Needham, "Identification of Ghost Tracks using a Likelihood Method," CERN, Geneva, Tech. Rep., 2008. [Online]. Available: https://cds.cern.ch/record/1107564.

[29] "Sim09 Generator Statistics." (), [Online]. Available: https://lhcbdoc.web.cern.ch/lhcbdoc/STATISTICS/SIM09STAT/index.shtml.

[30] V. Dedu, *Branching fraction measurement of* $\Lambda_b \rightarrow J/\Psi\Lambda$, Master's thesis, last accessed on 15 june 2024, Amsterdam, Nov. 2020. [Online]. Available: https://cds.cern.ch/record/2725393.

Appendices

Code

Location of the code:
https://github.com/timmeer03/bachelorthesis_s4907906

Weights

The ntuples taken into account for the weighting of MC data are the following:

`w_GBR_kinonly_LL`	`w_GBR_kinonly_DD`
`w_tracking_Pi_common_Default`	`w_tracking_P_common_Default`
`w_tracking_L1_common_Default`	`w_tracking_L2_common_Default`
`L1_wPIDEffCalib_Muon_nominal`	`L2_wPIDEffCalib_Muon_nominal`
`combined_wTrigL0_correction_nominal`	

Selection cut variables

The following selection cuts were imposed. Note that the transverse momentum of the pion and proton are not in the ntuples, they are constructed from x and y momentum which are in there. During the study of the high q^2 samples the `JPs` (below second horizontal line) version of the ntuples was used for all selections but `Lb_DTF_Lb_PV_ctau_0` and `Lb_DTF_Lb_PV_chi2_0`.

Selection		Value
`Lb_DTF_L0_PV_Lambda0_piplus_ID_0`	=	-211.0
`Lb_DTF_L0_PV_Lambda0_pplus_ID_0`	=	2212.0
`Lb_DTF_L0_PV_Lambda0_pplus_PT_0`	>	500
`Lb_DTF_L0_PV_Lambda0_piplus_PT_0`	>	500
`JPs_PT`	>	500
`Lb_DTF_L0_PV_Lambda0_M_0`	<	1115+20
`Lb_DTF_L0_PV_Lambda0_M_0`	>	1115-20
`Lb_DTF_Lb_PV_ctau_0`	<	100
`Lb_DTF_Lb_PV_chi2_0`	<	30
`Lb_DTF_L0_PV_M_0`	<	5740
`Lb_DTF_L0_PV_M_0`	>	5500
`Lb_DTF_L0_JPs_PV_Lambda0_piplus_ID_0`	=	-211.0
`Lb_DTF_L0_JPs_PV_Lambda0_pplus_ID_0`	=	2212.0
`Lb_DTF_L0_JPs_PV_Lambda0_pplus_PT_0`	>	500
`Lb_DTF_L0_JPs_PV_Lambda0_piplus_PT_0`	>	500
`Lb_DTF_L0_JPs_PV_Lambda0_M_0`	<	1115+20
`Lb_DTF_L0_JPs_PV_Lambda0_M_0`	>	1115-20
`Lb_DTF_L0_JPs_PV_M_0`	<	5500
`Lb_DTF_L0_JPs_PV_M_0`	>	5740

Data sets

Location of the data:

/eos/lhcb/wg/RD/Lb2Ll/RLambda/Tuples/v206/TupleProcess_MM_MVA/{sample}/{CL,MC}
{11,12,15,16,17,18}{LL,DD}{MU,MD}/{sample}_procTuple.root

Within each of the brackets one has to choose the sample, type of data, year, track-type and magnet polarization.

Finding suitable selections

For finding the selections all samples were simulation data (=MC) from 2018, had an LL track type and magnet-polarity MU. The following samples were imported :

`Lb2LMM`	`Lb2LJPsMM`
`Lb2L1520MM`	`Lb2L1520JPsMM`
`Xib02Xi0MM`	`Bd2KSJPsMM`
`Bd2KSMM`	`Xib2XiMM`

Obtaining efficiencies

For obtaining the efficiency there were two samples used: `Lb2LMM` & `Lb2LJPsMM`. The corresponding files are all combinations of (sample, year, track-type, magnet-polarity) for the years 2016/2017/2018, DD/LL and MU/MD. This resulted in twelve different files of simulation data for both `Lb2LMM` and `Lb2LJPsMM`.

Signal modeling

For signal modeling all the samples had an LL track. The same two simulated `Lb2LMM` & `Lb2LJPsMM` were once again used. Now with every combination of sample, year, LL, MU/MD. This resulted in six different simulation data files for both `Lb2LMM` and `Lb2LJPsMM`.

Detector data analysis

The detector data analysis part uses the same files as the ones used for obtaining efficiencies. But now instead of simulated `Lb2LMM` and `Lb2LJPsMM` files there is a `LPT` (real data) file. This means that there are 12 different files.

Rejecting backgrounds

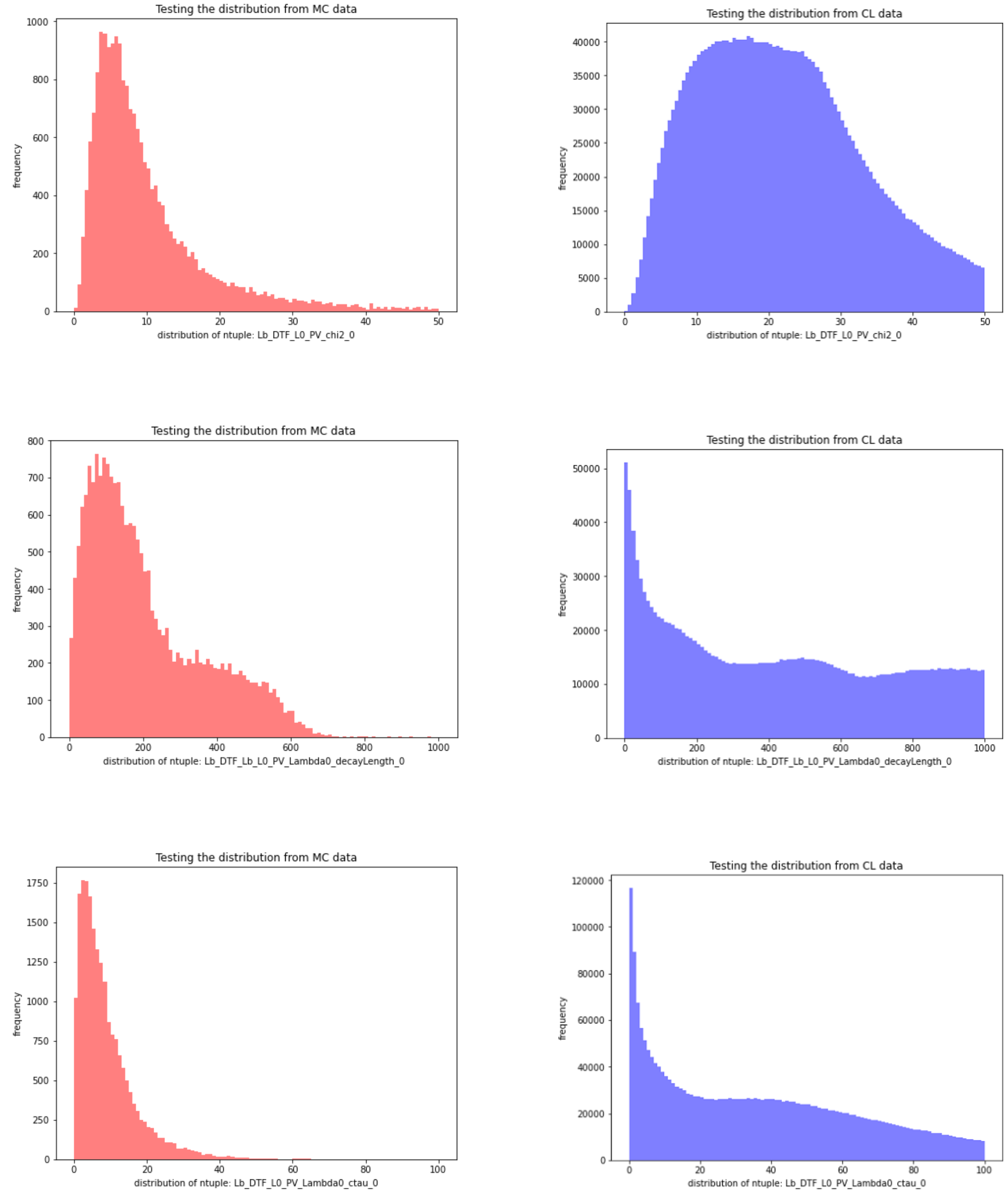

Figure 10: Comparison of simulation data against backgrounds. Note that the wrong label is on the vertical axis, the horizontal axis labels states the ntuple.